Collapse analysis of masonry bridges taking into account arch–fill interaction

Andrea Cavicchi, Luigi Gambarotta*

Department of Structural and Geotechnical Engineering, University of Genova, Via Montallegro, 1 - 16145 Genova, Italy

Abstract

Experimental collapse tests on full and model scale masonry bridges have shown that fill and spandrels can strongly affect the collapse behaviour and increase the load carrying capacity. To provide a structural description of the arch–fill interaction effects, a two-dimensional model of multi-span masonry bridges is developed in which arches and piers are described as beams made up of elastic, non-tensile resistant (NTR), ductile in compression material, and the fill as a Mohr–Coulomb material modified by a tension cut-off under plane strain conditions. The load carrying capacity is evaluated by a finite element limit analysis procedure based on the kinematic theorem. The fill domain is discretized by triangular elements connected by interface elements in order to allow possible velocity discontinuities at common sides of adjacent triangular elements; arches and piers are discretized by two-noded straight beam elements. By linearization of the limit domains in the generalized stress space, a linear programming problem is formulated and upper bounds of the collapse loads are obtained. Two examples are discussed, concerning a real single-span bridge, tested up to collapse, and a multi-span bridge. The ideal ductility assumption implicit in limit analysis is discussed by comparing the upper bound evaluations to the results obtained by incremental analysis in order to obtain the validity limits of the upper bound limit analysis for the proposed model.
© 2005 Elsevier Ltd. All rights reserved.

Keywords: Masonry bridges; Load carrying capacity; Arch–fill interaction; Limit analysis

1. Introduction

Several models for predicting the load carrying capacity of masonry bridges have been developed either only considering the vaults, modelled as plane arches, or also including arch–pier interaction. In both cases the assumption of non-tensile resistant (NTR) material for masonry is made. The solving procedures can be divided into two large categories corresponding to incremental methods and limit analysis. The former can be referred to in Castigliano [1] and the latter in the works of Kooharian [2] and Heyman [3], who extended the plastic limit analysis theorems to structural systems under the hypothesis of a rigid non-tensile resistant constitutive material model.

Experimental results obtained from collapse tests on full scale and model scale bridges [4,5] have shown the limits of the arch model for predicting the real behaviour of bridges, highlighting the strong influence of fill and spandrels on the collapse mechanism and the load carrying capacity. The growing need for assessing the real capacity of existing bridges has moved the research on to improving the above-mentioned methods in order to take into account the structural contribution of fill and spandrels. Structural modelling of the arch–fill interaction in mechanism analysis has been considered by Crisfield and Packam [6] and Hughes et al. [7], where the soil pressure is taken into account by applying additional horizontal forces to the arch; in the non-linear incremental FE models developed by Crisfield [8] and Choo et al. [9] the lateral response of the fill is modelled by one-dimensional horizontal elements having an elastic–ideal plastic constitutive equation with different responses at active and passive fill states.

* Corresponding author. Tel.: +39 010 353 2517; fax: +39 010 353 2534.
E-mail address: gambarotta@diseg.unige.it (L. Gambarotta).

In this paper a numerical procedure for the limit analysis of multi-span masonry bridges including the arch–fill interaction is developed on the basis of the kinematic theorem. The procedure is based on a two-dimensional finite element discretization of the masonry bridge [10]. Arches and piers are modelled as plane beams and the fill as a continuum under plane strain conditions. The fill is discretized by triangular elements and the arches and piers by two-noded beams characterized by two generalized hinges at the ends; four-noded interface elements connect adjacent triangular elements in order to allow localized strains along their edges, according to the Sloan and Kleeman approach [11]. Interface elements are also applied to allow displacement discontinuities between the fill and the arches at the extrados. The constitutive model assumed for arches and piers is non-tensile resistant (NTR) and ductile in compression, while the fill is modelled as a cohesive–frictional material according to the Mohr–Coulomb hypothesis with tension cut-off.

In order to evaluate the capability of the method for providing realistic results, a first example is discussed simulating a collapse test conducted on an existing single-span bridge [12]. The second example concerns a three-span bridge in which the suitability of the method for taking into account complex interactions between the arch–pier system and the fill is shown. The results obtained by assuming heavy and resistant fill are compared with the results obtained by assuming heavy but not resistant fill. This comparison points out the effect of the fill resistance on the collapse multiplier and the corresponding collapse mechanism. Moreover, the dependence of the load carrying capacity on the mechanical parameters of the fill and of the masonry is analysed.

The appreciable increase of the load carrying capacity provided by the fill corresponds to a different and higher demand for the arch strength resources. In particular, the increased exploitation of the masonry strength with its brittleness may turn out to be incompatible with the ideal ductility assumption implicit in the limit analysis theorems. In order to check this eventuality, in both examples an incremental analysis of the models is developed that allows us to check the ductility demand corresponding to the collapse mechanisms.

2. Structural model of the masonry bridge

Principal components of a typical masonry bridge are vaults, piers, haunchings, fill and spandrels, as shown in Fig. 1(a). With the aim of getting the most relevant effects of vault–fill interaction, in the present analysis a simple two-dimensional model is assumed (Fig. 1(b)) which considers the vaults, the piers and the fill as the resistant system, while it neglects the strengthening effect of the spandrels.

The fill is represented by the two-dimensional domain Ω_f under the hypothesis of plane strain. Vaults and piers are modelled as plane beams having rectangular cross section; the i-th beam occupies the two-dimensional region Ω_b^i

and is represented by its centreline $\mathscr{L}^i$. The plane strain assumption for the fill implies the displacement $\mathbf{u}(\mathbf{x}) = \{u_1(\mathbf{x}) \ u_2(\mathbf{x})\}^T$ at a point $\mathbf{x} = \{x_1 \ x_2\}^T \in \Omega_f$ to be contained in the plane (O, x_1, x_2) of the reference system, and the strain $\boldsymbol{\varepsilon}_f(\mathbf{x}) = \{\varepsilon_{11} \ \varepsilon_{22} \ \gamma_{12}\}^T$ to be represented by the in-plane components.

The displacements of points on a section of vaults and piers having the centroid located at point $\mathbf{x} \in \mathscr{L}^i$ depend on the displacement $\mathbf{u}(\mathbf{x})$ of the centroid and on the section rotation $\varphi(\mathbf{x})$. Within the Euler–Bernoulli hypothesis, the generalized strain is represented by vector $\boldsymbol{\varepsilon}_b(\mathbf{x}) = \{\varepsilon^a \ \chi\}^T$, ε^a being the axial strain at the centroid and χ the curvature. If a local reference frame $(\mathbf{t}, \mathbf{n})$ is introduced, $\mathbf{t}$ being the tangent and $\mathbf{n}$ the unit vectors normal to $\mathscr{L}^i$, the axial strain at the fibre on section $\mathbf{x}$ at a distance y from $\mathbf{x}$ along the unit vector $\mathbf{n}$ is $\varepsilon(\mathbf{x}, y) = \varepsilon^a(\mathbf{x}) - y\chi(\mathbf{x})$. The piers are commonly considered built in at the base, while the connection between the vault springings and the top of the piers is assumed rigid.

Moreover, displacement discontinuities between the vault extrados and the fill are allowed. With reference to the i-th beam section having the centroid at $\mathbf{x}$, the corresponding point at the extrados $\mathscr{I}^i$ is $\mathbf{x}^* = \mathbf{x} + \frac{h}{2}\mathbf{n}$, h being the beam section depth; the displacement jump at $\mathbf{x}^*$ is $[\![\mathbf{u}(\mathbf{x}^*)]\!] = \mathbf{u}_f(\mathbf{x}^*) - \mathbf{u}_b(\mathbf{x}^*)$, $\mathbf{u}_f(\mathbf{x}^*)$ being the displacement of the fill and $\mathbf{u}_b(\mathbf{x}^*) = \mathbf{u}(\mathbf{x}) - \varphi(\mathbf{x})\frac{h}{2}\mathbf{t}(\mathbf{x})$ the displacement at the extrados, which depends on the displacement $\mathbf{u}(\mathbf{x})$ and on the rotation $\varphi(\mathbf{x})$ at section $\mathbf{x}$. In the following, the normal $[\![u_n(\mathbf{x}^*)]\!] = \mathbf{n}^T[\![\mathbf{u}(\mathbf{x}^*)]\!]$ and the tangential $[\![u_t(\mathbf{x}^*)]\!] = \mathbf{t}^T[\![\mathbf{u}(\mathbf{x}^*)]\!]$ components of the velocity jump are collected in the strain vector of the interface $\boldsymbol{\varepsilon}^{\mathscr{I}}(\mathbf{x}) = \{[\![u_n]\!] \ [\![u_t]\!]\}^T$, $\mathbf{x} \in \mathscr{I}^i$.

The loads applied to the fill are the body force $\mathbf{b}(\mathbf{x})$, $\mathbf{x} \in \Omega_f$, representative of the weight per unit area of the fill, and the line force $\mathbf{p}(\mathbf{x})$, $\mathbf{x} \in \partial\Omega_f$, defined over the upper boundary $\partial\Omega_f$ corresponding to the free surface of the fill; $\mathbf{p}(\mathbf{x})$ is expressed as $\mathbf{p}(\mathbf{x}) = s\overline{\mathbf{p}}(\mathbf{x})$, $\overline{\mathbf{p}}(\mathbf{x})$ being a reference load and s a load multiplier. The stress field in the fill Ω_f is represented by the vector $\boldsymbol{\sigma}_f(\mathbf{x}) = \{\sigma_{11} \ \sigma_{22} \ \tau_{12}\}^T$ of the independent stress components. Line tractions act on the fill through the interfaces at the extrados of the vaults, represented by the normal σ_n and the tangential τ_n component in the local reference $(\mathbf{t}, \mathbf{n})$ collected in the interface stress vector $\boldsymbol{\sigma}_{\mathscr{I}}(\mathbf{x}) = \{\sigma_n \ \tau\}^T$, $\mathbf{x} \in \mathscr{I}^i$. Vaults and piers are subjected to external line forces $\mathbf{b}_b(\mathbf{x})$, $\mathbf{x} \in \mathscr{L}^i$, referred to the centroid of the section and representing the weight of the beam per unit length; externally applied couples are ignored. Line tractions and couples act on the arches as an effect of the line tractions applied through the extrados interface by the fill. Internal forces in arches and piers are represented by the axial N, shear T and bending M stress resultants referred to points of the beam centreline $\mathscr{L}$. From the Euler–Bernoulli hypothesis the generalized stress vector $\boldsymbol{\sigma}_b(\mathbf{x}) = \{N \ M\}^T$ at section $\mathbf{x} \in \mathscr{L}$ is defined.

The fill is assumed isotropic linear elastic–perfectly plastic having a yielding function corresponding to the
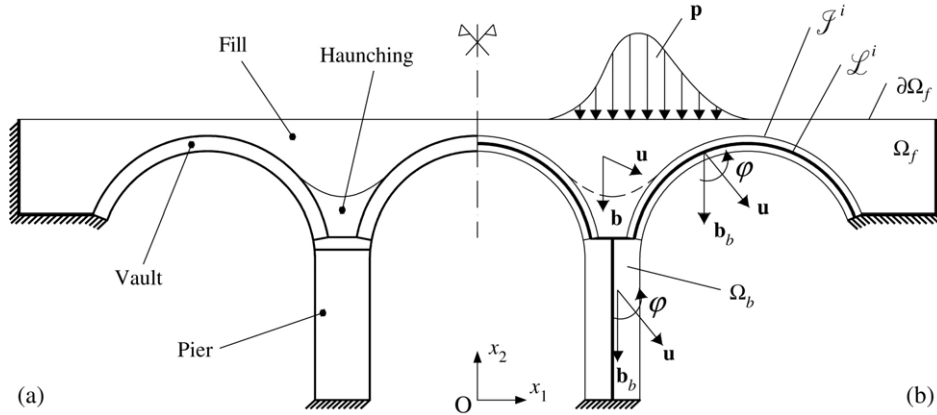
Fig. 1. (a) The bridge and its components; (b) the structural model of the bridge.

Mohr–Coulomb criterion under the plane strain assumption and modified by introducing a tension cut-off. The Mohr–Coulomb admissible domain is expressed by the inequality

$$f_c(\boldsymbol{\sigma}_f) = \sqrt{(\sigma_{11} - \sigma_{22})^2 + 4\tau_{12}^2} + (\sigma_{11} + \sigma_{22})\sin\varphi$$
$$- 2c\cos\varphi \leq 0, \tag{1}$$

c and φ being the cohesion and the angle of internal friction, respectively. The tension cut-off admissible domain is expressed by the inequality

$$f_t(\boldsymbol{\sigma}_f) = \sqrt{(\sigma_{11} - \sigma_{22})^2 + 4\tau_{12}^2} + (\sigma_{11} + \sigma_{22}) - 2\sigma_t$$
$$\leq 0 \tag{2}$$

where σ_t is the largest traction admitted.

In analogy, the displacement jump across the interfaces is ruled by the Coulomb admissible domain expressed by the inequality

$$f_c(\boldsymbol{\sigma}_{\mathscr{I}}) = |\tau| + \sigma_n \tan\varphi - c \leq 0, \tag{3}$$

together with the tension cut-off condition

$$f_t(\boldsymbol{\sigma}_{\mathscr{I}}) = \sigma_n - \sigma_t \leq 0. \tag{4}$$

The constitutive model of vaults and piers is obtained by assuming vanishing tensile resistance of the mortar joints orthogonal to the centreline of the vaults and piers. This follows the constitutive model of the beam section as elastic, non-tensile resistant (NTR) and ductile in compression (σ_c denotes the masonry compressive strength). Within the Euler–Bernoulli hypothesis, the constitutive model is expressed in terms of internal forces N and M, the axial strain ε^a and the curvature χ and is described by assuming monotonically increasing applied forces. Four different states can be recognized for the beam section, corresponding to the A, B, C and D regions shown in Fig. 2(b). Region A defines elastic states for which $M = EJ\chi$, $N = EA\varepsilon^a$, E, J and A being, respectively, the Young modulus, the centroidal moment of inertia and the area of the section. The stress states in region B define a partially cracked section with the compressed part still elastic; this region is defined by the
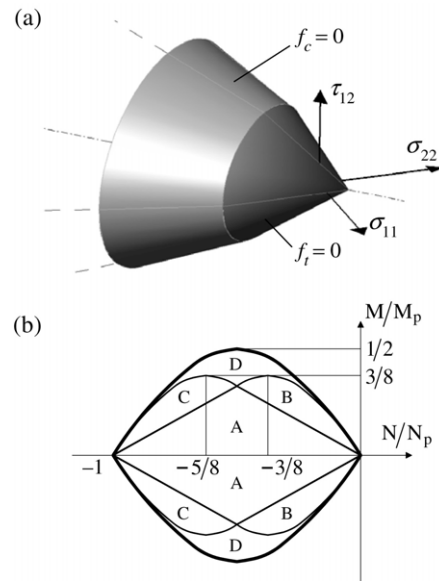
Fig. 2. (a) The Mohr–Coulomb limit domain modified by tension cut-off under the plane strain assumption; (b) the limit domain of the beam section under the hypothesis of elastic, non-tensile resistant, plastic in compression behaviour.

limits

$$-\frac{2}{3}\frac{N}{N_p} \leq \frac{|M|}{M_p} \leq -\frac{2N}{N_p}\left(1 + \frac{4}{3}\frac{N}{N_p}\right), \quad -\frac{1}{2} \leq \frac{N}{N_p} \leq 0,$$

where $N_p = hb|\sigma_c|$ and $M_p = \frac{1}{4}bh^2|\sigma_c|$; the corresponding constitutive equation at fixed axial force is

$$\frac{|M|}{M_p} = -\frac{2N}{N_p}\left(1 - \frac{2}{3}\sqrt{-\frac{1}{6}\frac{Nh}{|M_e(\chi)|}}\right), \tag{5}$$

where $M_e(\chi) = EJ\chi$. Region C, which is symmetric to region B with respect to axis $\frac{N}{N_p} = -\frac{1}{2}$ and is defined by the limits

$$-\frac{2}{3}\frac{\overline{N}}{N_p} \leq \frac{|M|}{M_p} \leq -\frac{2\overline{N}}{N_p}\left(1 + \frac{4}{3}\frac{\overline{N}}{N_p}\right), \quad -1 \leq \frac{N}{N_p} \leq -\frac{1}{2}$$
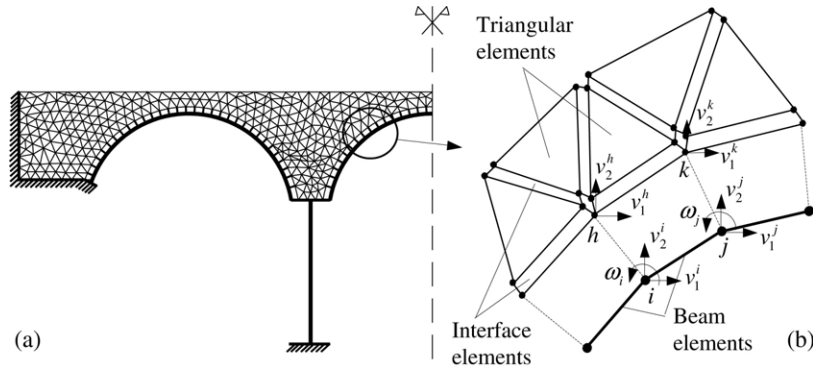
Fig. 3. (a) FE discretization of the model; (b) detail of the beam, triangular and interface elements assemblage.

$(\overline{N} = \sigma_c bh - N)$, defines stress states for which the section is completely compressed with a plastic portion; its constitutive equation is obtained by substituting $\overline{N}$ for N in (5). Finally, region D defines stress states for which the section exhibits both cracked and plastically compressed regions; this region is defined by the inequalities

$$-\frac{2N}{N_p}\left(1 + \frac{4}{3}\frac{N}{N_p}\right) \le \frac{|M|}{M_p} \le -\frac{2N}{N_p}\left(1 + \frac{N}{N_p}\right),$$

$$-\frac{1}{2} \le \frac{N}{N_p} \le 0$$

(if $-1 \le \frac{N}{N_p} \le -\frac{1}{2}$, in the left side N has to be replaced by $\overline{N}$), and the corresponding constitutive equation at fixed axial force is

$$\frac{|M|}{M_p} = -\frac{2N}{N_p}\left(1 + \frac{N}{N_p}\right) - \frac{1}{6}\left(\frac{1}{3}\frac{M_p}{M_e(\chi)}\right)^2. \tag{6}$$

The limit strength domain, i.e. the external limit envelope in Fig. 2(b), can be obtained from (6) for $\chi \to \infty$ and it is expressed by the equation

$$f_b(\boldsymbol{\sigma}_b) = \frac{|M|}{M_p} + \frac{2N}{N_p}\left(1 + \frac{N}{N_p}\right) = 0. \tag{7}$$

Finally, the ductility ratio

$$\delta(\mathbf{x}) = \frac{1}{\varepsilon_p}\min\left[\varepsilon_n\left(\mathbf{x} + \frac{h}{2}\mathbf{n}\right), \varepsilon_n\left(\mathbf{x} - \frac{h}{2}\mathbf{n}\right)\right]$$

at section $\mathbf{x} \in \mathscr{L}^i$ is defined.

3. FE evaluation of the load carrying capacity of the bridge

The complexity of the proposed model inhibits analytical solutions and evaluations of the collapse load and mechanism, so numerical solutions based on a finite element formulation must be pursued. To this end, the finite element discretization of the bridge based on beam, triangular and interface elements shown in Fig. 3(a) has been considered. Approximations of the load carrying capacity of the bridge can be achieved either by a standard non-linear incremental

analysis implemented in FE code (in this case LUSAS rel. 13.4 has been applied) or by using a numerical formulation based on the limit analysis theorems [13]. While the former provides information on the structural behaviour at intermediate states of the loading program, the latter does not require information about the elastic properties of the material considered in the model which are very often difficult to evaluate. Moreover, limit analysis is a more suitable tool for catching the collapse mechanism of the structural system.

In the next section, the FE discretization of the bridge is described; it allows one to evaluate an approximation of the collapse load and mechanism by an application of the upper bound theorem. To this end, velocity fields at incipient collapse will be considered and denoted as $\mathbf{v} = \dot{\mathbf{u}}$, $\omega = \dot{\varphi}$.

3.1. FE upper bound limit analysis

The fill domain Ω_f is discretized by three-noded triangular elements with six degrees of freedom, linear interpolation of the velocity field and a constant strain rate field. Four-noded interface elements connect the edges shared by the triangular elements in order to approximate possible discontinuities of the velocity field, according to Sloan and Kleeman [11] (Fig. 3(b)); the same elements are used to model the interfaces $\mathscr{I}$ at the extrados of arches.

In order to obtain a linear programming problem, the Mohr–Coulomb admissible domain assumed for the fill is approximated in the space of stress components by a tangent polyhedron having p_t faces defined, by analogy to Bottero et al. [14], by the inequalities

$$f_c^k(\boldsymbol{\sigma}) = \sigma_{11}(\sin\varphi + g_1(\vartheta_k)) + \sigma_{22}(\sin\varphi - g_1(\vartheta_k))$$
$$- \tau_{12}\sqrt{2}g_2(\vartheta_k) - 2c\cos\varphi \le 0, \ k = 1 \dots p_t, \tag{8}$$

where

$$g_1(\vartheta_k) = \frac{\cos\vartheta_k}{\sqrt{2\sin^2\vartheta_k + \cos^2\vartheta_k}},$$

$$g_2(\vartheta) = \frac{2\sin\vartheta_k}{\sqrt{2\sin^2\vartheta_k + \cos^2\vartheta_k}}, \qquad \vartheta_k = \frac{2\pi}{p_t}k. \tag{9}$$
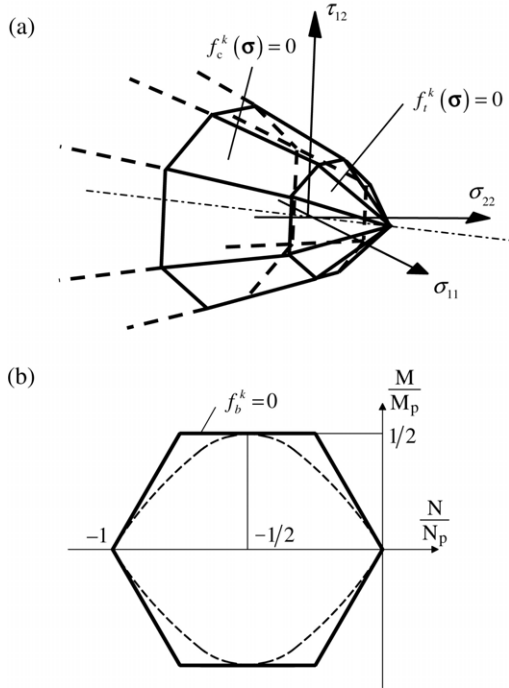
Fig. 4. Piecewise linearization of the admissible domains: (a) fill ($p_t = 8$); (b) generalized hinges ($p_b = 6$).

Analogously, the domain corresponding to the tension cut-off condition is linearized by a polyhedron tangent to the original domain having p_t faces, defined by the linear inequalities

$$f_t^k(\boldsymbol{\sigma}) = \sigma_{11}(1 + g_1(\vartheta_k)) + \sigma_{22}(1 - g_1(\vartheta_k))$$
$$- \tau_{12}\sqrt{2}g_2(\vartheta_k) - 2\sigma_t \leq 0, \ k = 1 \ldots p_t. \quad (10)$$

The resulting admissible domain in the stress space turns out to be the intersection of the polyhedra defined by inequalities (8) and (10), as shown in Fig. 4(a).

In order to apply the upper bound theorem, the associated flow rule is assumed. The uniform discrete strain rate field assumed in the triangular elements implies a uniform plastic flow through the element domain, that allows one to impose the flow rule only at a point of each triangular element. Inequalities (8) and (10) are prescribed over the element, so the yielding admissibility conditions are collected in the matrix form $\mathbf{f}^e = \mathbf{N}^e \boldsymbol{\sigma}^e - \mathbf{r}^e \leq \mathbf{0}$, from which the flow rule $\dot{\boldsymbol{\varepsilon}}^e = \mathbf{N}^{eT}\dot{\boldsymbol{\lambda}}^e$ follows, $\mathbf{N}^e(2p_t \times 3)$ being the matrix that collects the coefficients of the Eqs. (8) and (10) corresponding to the generalized stress vector $\boldsymbol{\sigma}^e = A^e\{\sigma_{11} \ \sigma_{22} \ \tau_{12}\}^T$, ($A^e$ is the element area), $\dot{\boldsymbol{\varepsilon}}^e = \{\dot{\varepsilon}_{11} \ \dot{\varepsilon}_{22} \ \dot{\gamma}_{12}\}^T$ the element strain rate vectors and $\dot{\boldsymbol{\lambda}}$ the $(2p_t \times 1)$ plastic multiplier vector. As a consequence, the power dissipated by the element is $D_p^e = \mathbf{r}^{eT}\dot{\boldsymbol{\lambda}}$.

The interface elements have four nodes and eight degrees of freedom (Fig. 5(a)). The two faces of the element correspond to the edges of the two triangular elements connected by the interface. The velocity field at each element face is obtained by linear interpolation of the corresponding
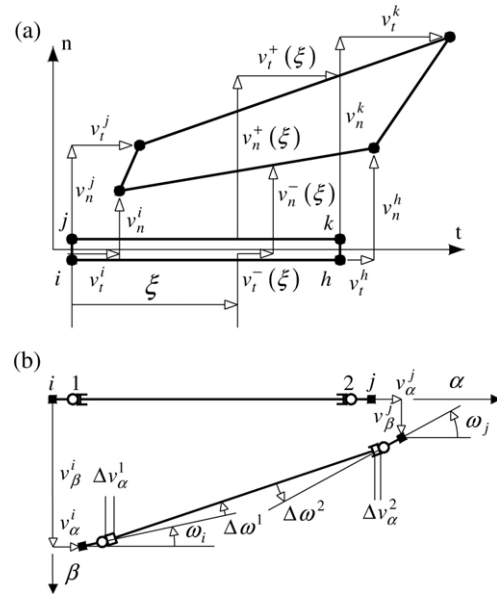
Fig. 5. (a) The interface element; (b) the beam element.

nodal velocities, in order to maintain compatibility with the velocity field of triangular elements. The nodal velocities are collected in the vector $\mathbf{v}^e = \{\mathbf{v}_i^e \ \mathbf{v}_j^e \ \mathbf{v}_h^e \ \mathbf{v}_k^e\}^T$, where $\mathbf{v}_q^e = \{v_1^q \ v_2^q\}^T$ ($q = 1 \ldots 4$) and v_1^q and v_2^q are the nodal velocity components of the q-th element node. The element velocity field is described by the vector $\mathbf{v}^T(\xi) = \{\mathbf{v}^{+T}(\xi) \ \mathbf{v}^{-T}(\xi)\}$, $\mathbf{v}^{\pm}(\xi) = \{v_n^{\pm} \ v_t^{\pm}\}^T$, where subscripts n and t denote the components in the local coordinate system, normal and tangent to the interface, respectively, superscripts $+$ and $-$ refer to the element faces and ξ is a local coordinate (Fig. 5(a)).

Local strain is described by the velocity jump $\dot{\boldsymbol{\varepsilon}}(\xi) = \{[[v_n(\xi)]] \ [[v_t(\xi)]]\}^T$, where $[[v_n(\xi)]] = v_n^+(\xi) - v_n^-(\xi)$ and $[[v_t(\xi)]] = v_t^+(\xi) - v_t^-(\xi)$, and depends on the nodal velocities via the compatibility equation $\dot{\boldsymbol{\varepsilon}}(\xi) = \mathbf{B}(\xi)\mathbf{v}^e$. The linearity of the generalized strain rate field allows the compatibility equations to be imposed only at the two end points of the element; defined by $\dot{\boldsymbol{\varepsilon}}^e = \{\dot{\boldsymbol{\varepsilon}}(0) \ \dot{\boldsymbol{\varepsilon}}(l)\}^T$ and $\mathbf{B}^e = \text{diag}[\mathbf{B}(0) \ \mathbf{B}(l)]$, l being the interface length, the element compatibility equation is expressed as $\dot{\boldsymbol{\varepsilon}}^e = \mathbf{B}^e\mathbf{v}^e$.

Defining the interface stress vector $\boldsymbol{\sigma}(\xi) = \{\sigma_n(\xi) \ \tau(\xi)\}^T$, collecting the resolved normal $\sigma_n(\xi)$ and tangential $\tau_n(\xi)$ stresses, the Coulomb admissible domain (3), expressed as two linear equations $f_{1,2}(\boldsymbol{\sigma}) = \pm\tau + \sigma_n \tan\varphi - c \leq 0$, and the tension cut-off condition (4) can be summarized in the local inequality $\mathbf{f}(\boldsymbol{\sigma}(\xi)) = \mathbf{N}\boldsymbol{\sigma}(\xi) - \mathbf{r} \leq \mathbf{0}$. This condition is specified at the end points of the interface, so yielding the element admissible domain as $\mathbf{f}^e(\boldsymbol{\sigma}^e) = \mathbf{N}^e\boldsymbol{\sigma}^e - \mathbf{r}^e \leq \mathbf{0}$, where $\boldsymbol{\sigma}^e = \frac{l}{2}\{\sigma_n(0) \ \tau_n(0) \ \sigma_n(l) \ \tau_n(l)\}^T$, with $\mathbf{N}^e = \frac{2}{l}\text{diag}[\ \mathbf{N} \ \mathbf{N} \ ]$ the (6×4) matrix of the vector normal to the faces of the limit domain and $\mathbf{r}^{eT} = \{\mathbf{r}^T \ \mathbf{r}^T\}$. The corresponding associated flow rules are $\dot{\boldsymbol{\varepsilon}}(\xi) = \mathbf{N}^T\dot{\boldsymbol{\lambda}}(\xi)$ and $\dot{\boldsymbol{\varepsilon}}^e = \mathbf{N}^{eT}\dot{\boldsymbol{\lambda}}^e$, respectively, where the vector $\dot{\boldsymbol{\lambda}}(\xi)$ represents the plastic multiplier rate field at the interface and

$\dot{\boldsymbol{\lambda}}^e = \{\dot{\boldsymbol{\lambda}}(0) \;\; \dot{\boldsymbol{\lambda}}(l)\}^T$ collects the corresponding values at the end points. Since the linearity of the deformation rate field $\dot{\boldsymbol{\varepsilon}}(\xi)$ implies the linearity of the field $\dot{\boldsymbol{\lambda}}(\xi)$ over the interface, the power dissipated by the interface is

$$D_p = \int_l \dot{\boldsymbol{\varepsilon}}^T(\xi)\boldsymbol{\sigma}(\xi)\mathrm{d}\xi = \mathbf{r}^T \int_l \dot{\boldsymbol{\lambda}}(\xi)\mathrm{d}\xi = \frac{l}{2}\mathbf{r}^T(\dot{\boldsymbol{\lambda}}(l) + \dot{\boldsymbol{\lambda}}(0))$$
$$= \mathbf{r}^{eT}\dot{\boldsymbol{\lambda}}^e. \tag{11}$$

Two-noded, straight beam elements are assumed whose deformation depends on two generalized hinges located at the end sections, allowing relative localized axial Δv_α^m and rotational $\Delta \omega^m$ ($m = 1, 2$) velocities (Fig. 5(b)), collected at each end section in the generalized strain rate vector $\dot{\boldsymbol{\varepsilon}} = \{\Delta v_\alpha \;\; \Delta \omega\}^T$. The generalized beam element strain rate $\dot{\boldsymbol{\varepsilon}}^e = \{(\Delta v_\alpha^1 + \Delta v_\alpha^2) \;\; \Delta \omega^1 \;\; \Delta \omega^2\}^T$ is assumed, where we have introduced the total axial relative velocity $(\Delta v_\alpha^1 + \Delta v_\alpha^2)$ which depends, via the compatibility equation $\dot{\boldsymbol{\varepsilon}}^e = \mathbf{B}^e \mathbf{v}^e$, on the nodal velocity vector of the element $\mathbf{v}^{eT} = \{\mathbf{v}_i^{eT} \;\; \mathbf{v}_j^{eT}\}$, $\mathbf{v}_k^e = \{v_1^k \;\; v_2^k \;\; \omega^k\}^T$.

The activation of a generalized hinge depends on the admissible domain of a rectangular section made up of non-tensile resistant and ductile in compression material (Fig. 2(b)). This domain, defined in the space of axial and bending stress components, is discretized by the tangent polygon resulting as the envelope of the linear inequalities

$$f_b^{h\pm}(N, M) = \pm\frac{M}{M_p} - \frac{2}{(p_b - 2)^2}\left[4(R-1)^2\right.$$
$$\left. - \frac{N}{N_p}(p_b - 2)(p_b + 2 - 4R)\right] \le 0, \; R = 1 \ldots \frac{p_b}{2}, \tag{12}$$

where p_b is the number of sides of the polygon (Fig. 4(b)).

By assuming uniform axial force N, the element generalized stress vector $\boldsymbol{\sigma}^e = \{N \;\; M_1 \;\; M_2\}^T$ is defined, M_1 and M_2 being the bending moments at the end sections; the admissible domains (12) are collected in the inequality $\mathbf{f}^e = \mathbf{N}^e\boldsymbol{\sigma}^e + \mathbf{r}^e \le \mathbf{0}$ and the associated flow rule $\dot{\boldsymbol{\varepsilon}}^e = \mathbf{N}^{eT}\dot{\boldsymbol{\lambda}}^e$ is assumed, $\mathbf{N}^e(2p_b \times 3)$ being the matrix of the coefficients in (12) and $\dot{\boldsymbol{\lambda}}^e$ the vector that collects the $2p_b$ plastic multiplier rate at the two hinges. Finally, the power dissipated by the beam is obtained as the sum of the contributions provided by each active hinge and is expressed as $D_p = \boldsymbol{\sigma}^{eT}\dot{\boldsymbol{\varepsilon}}^e = \mathbf{r}^{eT}\dot{\boldsymbol{\lambda}}^e$. It is worth noting that the dissipation at the generalized hinge ruled by the limit domain (7) only depends on ductile compressive strain, since cracking of NTR materials is not a dissipative mechanism; this section property is only approximated when the approximation (12) is applied.

The finite element model is represented by the admissible domains of the elements summarized in the inequality $\mathbf{f} = \mathbf{N}\boldsymbol{\sigma} - \mathbf{r} \le \mathbf{0}$, where $\boldsymbol{\sigma}$ is the vector of all the element generalized stress components, and by the vector $\dot{\boldsymbol{\varepsilon}}$ of the generalized strain rate components expressed by the associated flow rule $\dot{\boldsymbol{\varepsilon}} = \mathbf{N}^T\dot{\boldsymbol{\lambda}}, \dot{\boldsymbol{\lambda}} \ge \mathbf{0}$, $\dot{\boldsymbol{\lambda}}$ being the plastic multiplier vector. By the global compatibility equations

$\dot{\boldsymbol{\varepsilon}} = \mathbf{Ba}$, involving the nodal velocity vector $\mathbf{a}$ and the assembled compatibility matrix $\mathbf{B}$, the standard linear conditions on vectors $\mathbf{a}$ and $\dot{\boldsymbol{\lambda}}$ are obtained:

$$\mathbf{Ba} - \mathbf{N}^T\dot{\boldsymbol{\lambda}} = \mathbf{0}, \qquad \dot{\boldsymbol{\lambda}} \ge \mathbf{0}. \tag{13}$$

The external and internal kinematical constraints are summarized by the homogeneous linear equation

$$\mathbf{Aa} = \mathbf{0}, \tag{14}$$

where matrix $\mathbf{A}$ depends on the boundary conditions on the velocity field and on the location and topological properties of the internal rigid links. Moreover, the dissipation rate D_p of the mechanism represented by vectors $\mathbf{a}$ and $\dot{\boldsymbol{\lambda}}$ is obtained as $D_p = \mathbf{r}^T\dot{\boldsymbol{\lambda}}$, the sum of the contributions of all active element mechanisms.

The applied loads are reduced to nodal forces and collected in the nodal load vector $\mathbf{q} = \mathbf{q}_0 + s\overline{\mathbf{q}}$, obtained as the sum of the contributions of the dead load vector $\mathbf{q}_0$ and the live load vector $s\overline{\mathbf{q}}$, s being the unknown collapse load multiplier. Denoting the power of the external dead loads as $P_e = \mathbf{q}_0^T\mathbf{a}$ and imposing the normalizing condition implying the positivity of the power of live loads

$$\overline{\mathbf{q}}^T\mathbf{a} = 1, \tag{15}$$

the kinematically admissible multiplier s_k is expressed in the standard form as the difference between the power dissipated by the elements and the power of the external dead loads:

$$s_k = -P_e + D_p = \{-\mathbf{q}_0^T \;\; \mathbf{r}^T\}\begin{Bmatrix}\mathbf{a} \\ \dot{\boldsymbol{\lambda}}\end{Bmatrix}. \tag{16}$$

Finally, the collapse multiplier upper bound s_u relating to the finite element model considered is obtained as the solution of the linear programming problem

$$\begin{cases} s_u = \min(-P_e + D_p) = \min\{-\mathbf{q}_0^T \;\; \mathbf{r}^T\}\begin{Bmatrix}\mathbf{a} \\ \dot{\boldsymbol{\lambda}}\end{Bmatrix}, \\ \begin{bmatrix}\mathbf{A} & \mathbf{0} \\ \overline{\mathbf{q}}^T & \mathbf{0} \\ \mathbf{B} & -\mathbf{N}^T\end{bmatrix}\begin{Bmatrix}\mathbf{a} \\ \dot{\boldsymbol{\lambda}}\end{Bmatrix} = \begin{Bmatrix}\mathbf{0} \\ 1 \\ \mathbf{0}\end{Bmatrix}, \\ \dot{\boldsymbol{\lambda}} \ge \mathbf{0}, \end{cases} \tag{17}$$

where the feasible domain imposes the compatibility conditions (13), (14) and Eq. (15); the vectors $\mathbf{a}$ and $\dot{\boldsymbol{\lambda}}$ that minimize the load multiplier define an approximation of the collapse mechanism, depending on the finite element discretization.

4. Examples

4.1. Example 1: Prestwood bridge

In order to evaluate the capability of the procedure for predicting the collapse behaviour of real bridges, the first example relates to Prestwood bridge [12], a single-span bridge tested to collapse within the experimental research
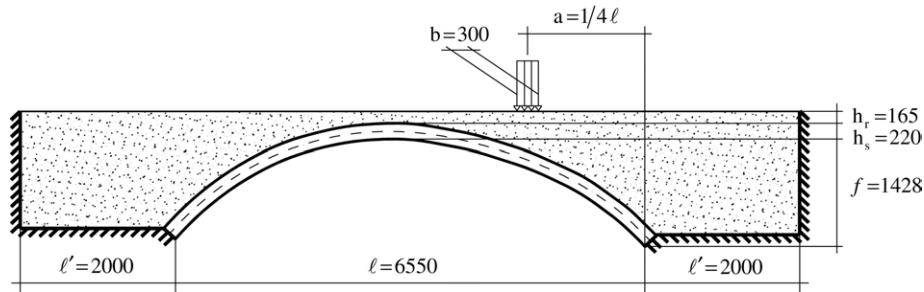
Fig. 6. Geometry of the model (mm).

on masonry bridges supported by the Transport Research Laboratory (TRL).

The vault shape, having span $\ell = 6550$ mm and upper rise $f = 1428$ mm, is distorted from the originally segmental shape. The vault thickness is $h_s = 220$ mm and comprises a single ring of bricks laid as headers; the fill depth at the crown is $h_r = 165$ mm and the total bridge width is 3800 mm. The live load was $b = 300$ mm wide and was applied across the bridge at quarter-span (Fig. 6). The fill density is $\gamma_f = 20$ kN/m^3 and the masonry density is $\gamma_m = 20$ kN/m^3.

The experimental collapse mechanism of the bridge is shown in Fig. 7. The vault collapse mechanism exhibits four hinges that are clearly visible in the picture; the mechanism developed with negligible material crushing. The arch mechanism constrains the fill region under the applied load to move downward and the fill at the other side of the bridge to move upward; the experimental collapse load was $P_{\exp} = 228$ kN.

In Fig. 8 the collapse mechanism resulting from the numerical limit analysis is shown, obtained by assuming compressive strength $\sigma_c = 4.5$ MPa for the arch masonry and angle of internal friction $\varphi = 37°$ (see Ref. [4]) and cohesion $c = 10$ kPa for the fill. The small black circles on the arch ring represent the active hinges, while the greyscale in the fill domain denotes different values of the ratios between the principal shear strain rate at each element and the maximum in the fill.

As in the experimental test, in the numerical collapse mechanism four groups of hinges develop. The loaded side of the arch moves downward, and the arch mechanism pushes the left side; as a consequence, the fill over the left side is moved upward. The first hinge on the left side of the arch does not develop at the springing, as happens in the arch where the fill is heavy but not resistant; the presence of the fill constrains the hinge to move upward. This behaviour agrees with the experimental result shown in Fig. 7.

The diagrams in Fig. 9(a), obtained by assuming an internal friction angle $\varphi = 37°$ and a compressive strength of the arch $\sigma_c = 4.5$ MPa, show the influence of the fill cohesion c on the collapse load; the lower line corresponds to the value obtained assuming no resistant fill, $P_u = 46.2$ kN. Assuming $c = 1$ kPa, the collapse load is

$P_u = 149.1$ kN, about 65% of the experimental value $P_{\exp} = 228$ kN, which is obtained numerically assuming $c = 10$ kPa. The diagrams in Fig. 9(b), obtained assuming the internal friction angle $\varphi = 37°$ and cohesion $c = 10$ kPa, show the influence of the compressive strength of the arch on the collapse load; the value obtained assuming unlimited compressive strength is $P_u = 267.9$ kN, which is about 17% higher than the value obtained assuming $\sigma_c = 4.5$ MPa, $P_u = 228.0$ kN; the corresponding values obtained assuming no resistant fill are $P_u = 57$ kN and $P_u = 46.2$ kN respectively.

The strengthening effects of the fill correspond to a higher exploitation of the strength resources of the arch; in particular, the development of the collapse mechanism predicted by the limit analysis requires the development of plastic compressive strains higher than those predicted by simplified models without fill resistance that could be no longer consistent with the masonry behaviour. The diagrams in Fig. 10 show the load–deflection curve (referred to the vertical displacement of the section at the load position) obtained by the incremental analysis, compared to the upper bound obtained by limit analysis; the different collapse loads corresponding to different ductility δ values are shown. The results are obtained by assuming $\sigma_c = 4.5$ MPa, $c = 10$ kPa and $\varphi = 37°$; the elastic moduli assumed for masonry and fill in the incremental analysis are $E_m = 15\,000$ MPa and $E_f = 300$ MPa, respectively.

The section of the arch that first reaches the compressive elastic limit is located under the area where the load is applied; the corresponding load step is indicated by $\delta = 1$ in the diagram of Fig. 10. The difference between the results provided by the incremental analysis with $\delta \leq 2$ and the upper bound estimated from limit analysis is about 13%.

In this case the effect of a limitation of ductility on the development of the collapse mechanism is limited. This result agrees with the experimental behaviour of the bridge and shows that limit analysis can be applied with a good approximation.

4.2. Example 2: A multi-span bridge

The second example relates to a three-span bridge having circular arches, thickness $h_s = 1$ m, span $\ell = 14$ m and span to rise ratio $f/\ell = 2$. The height of the piers is $h = 10$ m and

Fig. 7. The Prestwood bridge: the collapse mechanism.
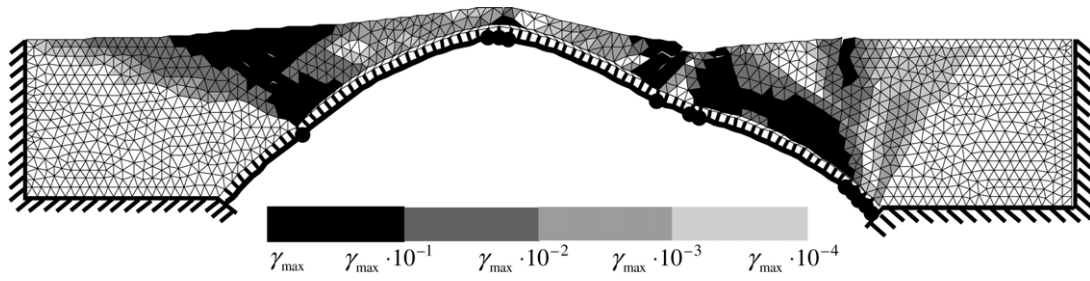
Fig. 8. The collapse mechanism of the Prestwood bridge FE model.
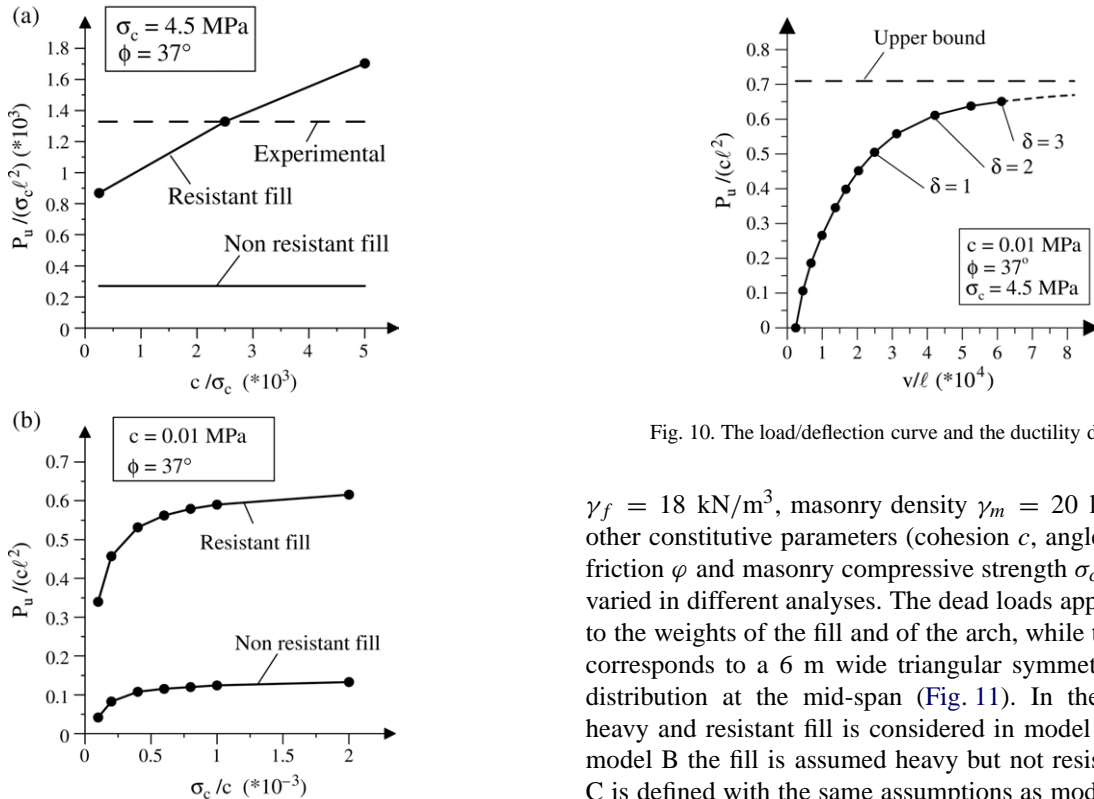
Fig. 10. The load/deflection curve and the ductility demand.

Fig. 9. The influence (a) of the cohesion and (b) of the angle of internal friction on the collapse load.

the thickness is $h_p = 3$ m; the depth of fill at the crown is $h_r = 1$ m. The assumed material parameters are: fill density

$\gamma_f = 18$ kN/m^3, masonry density $\gamma_m = 20$ kN/m^3. The other constitutive parameters (cohesion c, angle of internal friction φ and masonry compressive strength σ_c) have been varied in different analyses. The dead loads applied are due to the weights of the fill and of the arch, while the live load corresponds to a 6 m wide triangular symmetric pressure distribution at the mid-span (Fig. 11). In the following, heavy and resistant fill is considered in model A, while in model B the fill is assumed heavy but not resistant; model C is defined with the same assumptions as model B but the haunching, which is modelled as a rigid body.

In Fig. 11 the collapse mechanism of model A is shown, where the arch–pier–fill interaction is clearly represented. The failure mechanism of the arch–pier system is characterized by thirteen groups of hinges attained at the
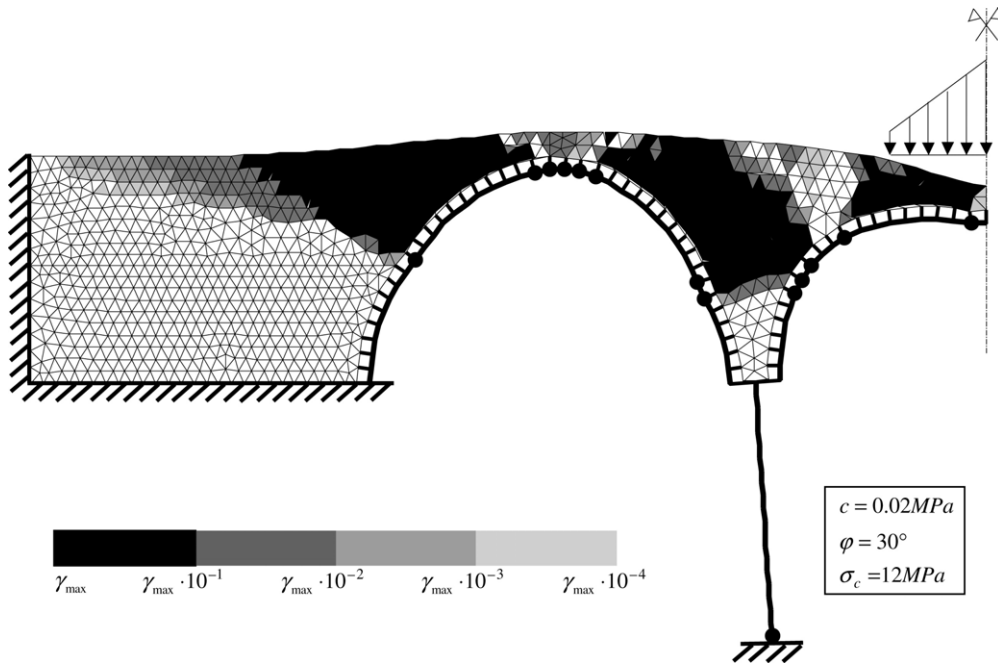
Fig. 11. The collapse mechanism of the three-span bridge (model A).

crowns and at the haunches of the arches and at the bottom sections of the piers. In the region close to the springings the presence of the fill constrains the haunches and inhibits the hinge activation; in particular, the haunchings remain rigid even though they have been assumed to have the same material parameters as the fill.

The mechanism developed allows the crown of the central arch to move downward, imposing the rotation of the piers and the contraction of the lateral arches in which the crowns move upward; a compatible inelastic deformation field is attained in the fill, which is constrained to move upward. Inelastic sliding is spread over a large region of the fill that extends beyond the ends of the external arches. In Figs. 12(a) and (b) the collapse mechanisms of model B and model C are shown, respectively; the collapse mechanism of model B is limited to the central arch, so it behaves as a single-arch bridge.

The diagrams in Fig. 13 show the dependence of the load carrying capacity on the compressive strength in models A and C. The values from model A turn out to be about 2 times as great as the corresponding values of model C. The diagrams in Fig. 14(a) and (b) show the dependence of the load carrying capacity on the values of the cohesion and of the angle of internal friction in model A; the lower line corresponds to model C.

The results obtained show that the FE limit analysis procedure is able to solve complex models, but the validity of the ideal ductility hypothesis has to be verified. In Fig. 15 the load/deflection diagram (referred to the vertical displacement of the mid-span section) obtained by the incremental analysis is shown, compared to the upper bound obtained by limit analysis. The results have been obtained
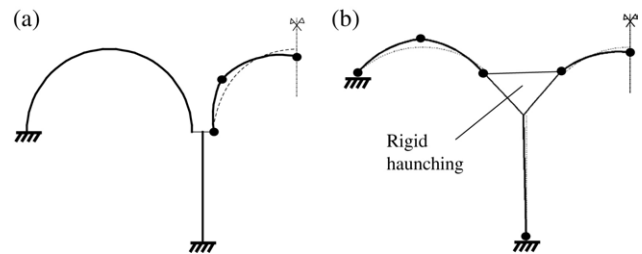
Fig. 12. The collapse mechanisms of model B (a) and model C (b).
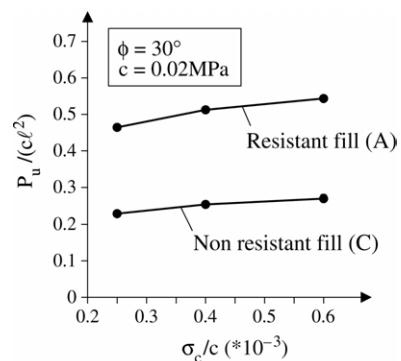
Fig. 13. The influence of the masonry compressive strength on the collapse load.

by assuming $\sigma_c = 12$ MPa, $c = 20$ kPa and $\varphi = 30°$; the masonry and fill elastic moduli assumed for the incremental analysis are $E_m = 15\,000$ MPa and $E_f = 300$ MPa, respectively.

The limit $\delta = 2$ is reached in the central arch at the mid-span section; the difference between the results provided by

(a)

(b)
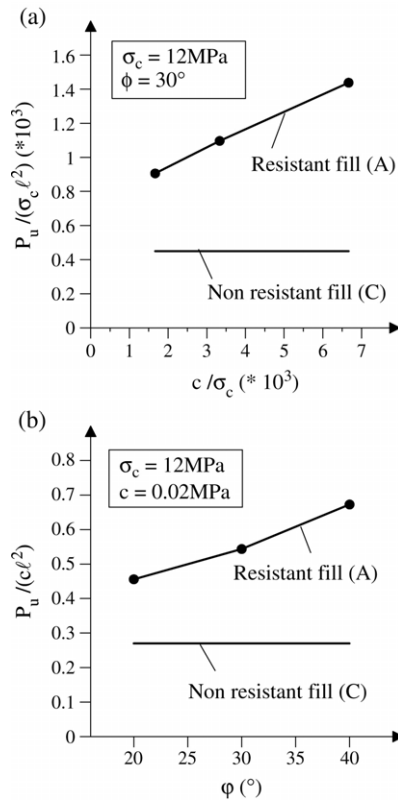
Fig. 14. The influence of the cohesion (a) and of the angle of internal friction (b) of the fill on the collapse load.

Fig. 15. The load/deflection curve and ductility demand.

the incremental analysis with $\delta \leq 2$ and the upper bound estimated from limit analysis is about 9%.

5. Conclusions

The structural model and the numerical procedure proposed here, which is based on the kinematic theorem of limit analysis, provide upper bounds of the collapse load and the corresponding collapse mechanisms of masonry bridges taking into account arch–fill interaction. Two examples are considered in order to show the capabilities of the FE approach and the strong influence of the fill on the bridge strength. In particular, the first example concerning a real bridge tested to collapse has provided a good simulation of the experimental results. The second example relating to a multi-span bridge has shown the capability of the procedure for representing the complex interaction between piers, arches and fill at collapse. The effect of a limitation of the masonry ductility has been analysed by developing a reference incremental analysis of both the example models described. The results obtained show that the collapse mechanisms can develop almost completely even if the ductility is limited, demonstrating that limit analysis can still be used successfully.

The approximations introduced have allowed us to define a simplified model able to describe some relevant aspects of the arch–fill interaction requiring less cumbersome

numerical analysis. On the other hand, the model presents some limitations that have to be taken into account. The plane strain assumption for the fill corresponds to assuming the spandrels to be providing perfect smooth boundary conditions; the effects of this assumptions have to be evaluated and depend on the geometry of the bridge. Moreover, a more realistic description of the development of passive and active fill pressures at the arch extrados needs to take account of different corresponding displacements that are larger in the latter case. Finally, the numerical representation of discontinuities in the velocity field that characterizes the solutions of collapse problems assuming perfect plasticity is still an open problem; the interface elements used allow discontinuities to develop but their directions are arbitrarily fixed by the triangular element shape.

Acknowledgement

References

[1] Castigliano CAP. Theorie de l'equilibre des systemes elastiques et ses applications. Torino: Augusto Federico Negro; 1879;
Andrews ES. Elastic stresses in structures [Andrews Trans.]. London: Scott Greenwood & Son; 1919.

[2] Kooharian A. Limit analysis of Voussoir (segmental) and concrete arches. Proc Am Concr Inst 1953;89:317–28.

[3] Heyman J. The stone skeleton. Internat J Solids Structures 1966;2: 249–79.

[4] Page J. Masonry arch bridges—TRL state of the art review. HMSO; 1993.

[5] Royles R, Hendry AW. Model tests on masonry arches. Proc Inst Civ Eng, Part 2 1991;91:299–321.

[6] Crisfield MA, Packam AJ. A mechanism program for computing the strength of masonry arch bridges. Research report 124. Crowthorne: Transport Research Laboratory; 1985.

[7] Hughes TG, Hee SC, Soms E. Mechanism analysis of single span masonry arch bridges using a spreadsheet. Proc Inst Civ Eng Struct Build 2002;152:341–50.

[8] Crisfield MA. Finite element and mechanism methods for the analysis of masonry and brickwork arches, Research report 19. Crowthorne: Transport Research Laboratory; 1985.

[9] Choo BS, Coutie MG, Gong NG. Finite element analysis of masonry arch bridges using tapered elements. Proc Inst Civ Eng, Part 2 1991; 91:755–70.

[10] Cavicchi A. Analisi limite agli elementi finiti di archi murari interagenti con il riempimento per la valutazione della capacità portante di ponti in muratura. Ph.D. thesis. Italy: Department of Structural and Geotechnical Engineering, University of Genova; 2004.

[11] Sloan SW, Kleeman PW. Upper bound limit analysis using discontinuous velocity fields. Comput Methods Appl Mech Engrg 1995;127:293–314.

[12] Page J. Load tests to collapse on two arch bridges at Preston, Shropshire and Prestwood, Staffordshire. Department of Transport, TRRL Research report 110. Crowthorne (England): TRL; 1987.

[13] Jirásek M, Bažant ZP. Inelastic analysis of structures. Chichester: J. Wiley & Sons; 2002.

[14] Bottero A, Negre R, Pastor J, Turgeman S. Finite element method and limit analysis theory for soil mechanics problems. Comput Methods Appl Mech Engrg 1980;22:131–49.